Volume 13 | Number 2 | 20 January 2026

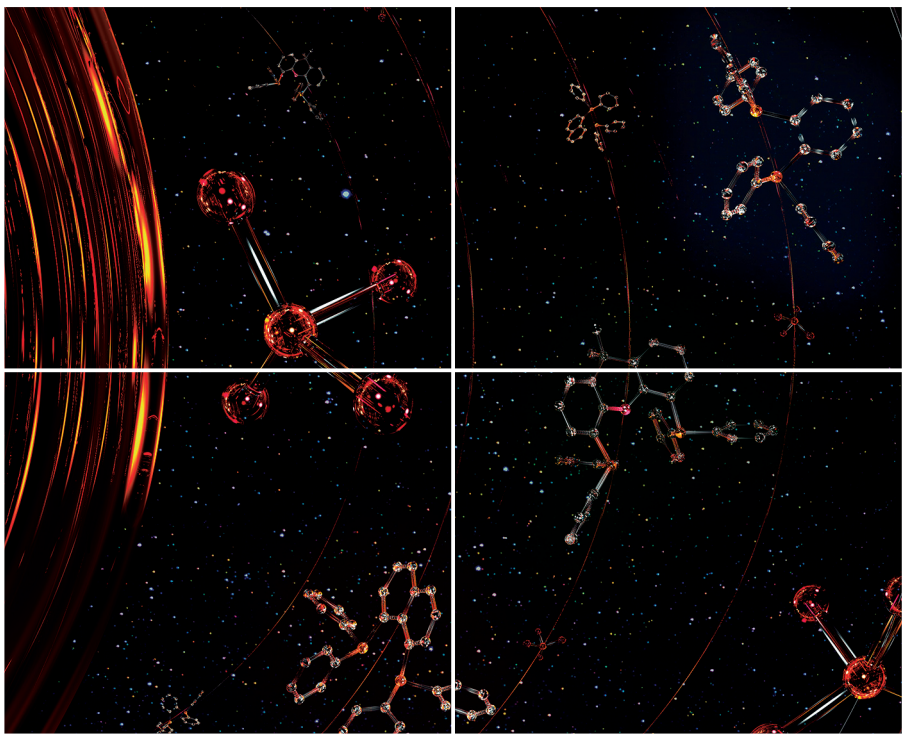

INORGANIC CHEMISTRY

FRONTIERS

CCS 中国化学会 CHINESE CHEMICAL SOCIETY

PEKING UNIVERSITY 1898

ROYAL SOCIETY OF CHEMISTRY

rsc.li/frontiers-inorganic

INORGANIC CHEMISTRY FRONTIERS

RESEARCH ARTICLE

View Article Online
View Journal | View Issue

Cite this: *Inorg. Chem. Front.*, 2026, **13**, 377

The role of the electron density of the acceptor in efficient diphenylphosphino-gold(I) TADF emitters

Oliver Baltar, [a] Inés Soldevilla,[a] Rinat T. Nasibullin,[b] Rashid R. Valiev,[b] M. Elena Olmos, [a] Miguel Monge, [a] Dage Sundholm, [b] María Rodríguez-Castillo *[a] and José M. López-de-Luzuriaga *[a]

We report the synthesis of a series of diphosphino-gold(I) complexes (**1–4**) using the *cis*-1,2-bis(diphenylphosphino)ethylene (dppe), 1,2-bis(diphenylphosphino)benzene (dppBz), 4,5-bis(diphenylphosphino)-9,9-dimethylxanthene (Xantphos) and 1,8-bis(diphenylphosphino)naphthalene (dppn) chelating ligands in combination with the [Au(C_6F_5)(tht)] precursor. The bis(diphosphine)-gold(I) complexes are designed for investigating how thermally activated delayed fluorescence (TADF) depends on the ligand. The emission wavelength of the intense luminescent emissions of **2**, **3** and **4** at room temperature (RT) and at 77 K is modulated by the electronic nature of the ligands. Temperature-dependent lifetime measurements and computational studies suggest that **2**, **3** and **4** exhibit TADF at RT. Rate constants of intersystem crossing (ISC) and reverse ISC (RISC) were calculated at the ADC(2) level using an ONIOM approach to consider solid-state environmental effects on the molecular structures and spin–orbit coupling matrix elements calculated at the density functional theory (DFT) level. The photophysical studies show that the observed RT emissions arise from TADF with contributions in the range of 67–84% depending on the diphosphine ligand.

Received 5th August 2025,
Accepted 13th November 2025

DOI: 10.1039/d5qi01661d

rsc.li/frontiers-inorganic

Introduction

The design of a new generation of emitters based on thermally activated delayed fluorescence (TADF) has been driven mainly by the ongoing search for materials with higher quantum efficiency, a key requirement for their application in electroluminescent devices.

Various studies have provided a basic understanding of the criteria that complexes must meet to exhibit TADF behaviour that is suitable for practical applications.[1–3]

A key requirement is that the materials must have short decay times to reduce device stability problems and roll-off effects. To achieve this goal, molecules incorporating electron donor (D) and acceptor (A) groups have traditionally been designed to promote charge transfer transitions, resulting in TADF behaviour and shorter lifetimes compared to the previous generation of phosphorescent emitters.

In terms of energies, it is essential that there is a small energy difference ($\Delta E(S_1–T_1)$) between the lowest singlet (S_1) and triplet (T_1) excited states. This condition is fulfilled by molecules with a small HOMO–LUMO overlap. To structurally reach this goal, two main strategies are usually employed: rotating the D and A units around the D–A axis, which produces orthogonal D–A relative orientations, or increasing the D–A distance by implementing a longer bridge.[4–8] The small difference between the two states ideally allows thermal energy at room temperature to pass between the T_1 and S_1 states. In addition, a fast radiative rate constant between the S_1 and S_0 states is also required, which reduces the decay time.[4,5,9] However, fulfilling both conditions in the same molecule can be counterproductive, since achieving a low $\Delta E(S_1–T_1)$ with minimal overlap between HOMO and LUMO can simultaneously result in small transition dipole moments and, consequently, a small radiative rate constant $k(S_1–S_0)$.[4,5]

On the other hand, although the incorporation of heavy metals into these molecules promotes intersystem crossing (ISC) as a result of increased spin–orbit coupling (SOC), rapid radiative inverse intersystem crossing (RISC) is also important for the TADF process. The key factor for maximizing the RISC rate constant is a small $\Delta E(S_1–T_1)$ as shown in eqn (1). Therefore, understanding how to minimize this difference through appropriate molecular design is an important challenge.[10]

$$k_{RISC} = k_{ISC}\, e^{-\Delta E(S_1–T_1)/k_B T} \quad (1)$$

The metals most commonly used in complexes exhibiting TADF are Cu and Ag, as they are less expensive alternatives to

[a]*Departamento de Química, Instituto de Investigación en Química de la Universidad de La Rioja (IQUR), Universidad de La Rioja, Complejo Científico Tecnológico, 26006-Logroño, Spain. E-mail: josemaria.lopez@unirioja.es, maria.rodriguez@unirioja.es*
[b]*Department of Chemistry, Faculty of Science, University of Helsinki, P.O. Box 55, (A. I. Virtasen aukio 1), FIN-00014, Finland*

Pt and Ir. However, although low-energy localized triplet excited states, which could increase the singlet–triplet gap and reduce efficiency, have not been reported in Cu(I) complexes, its inherent susceptibility to oxidation remains a significant drawback. Similarly, the Ag(I) analogues often exhibit photosensitivity and poor luminescent properties. These problems seriously compromise the stability and efficiency of light-emitting-diode (LED) devices in which these metals are incorporated.

Recently, in our laboratory, we have observed TADF processes in gold-containing complexes of stoichiometries [AuR(dppBz)] (R = C_6F_5, $C_6Cl_2F_3$, C_6Cl_5, C_6BrF_4, C_6F_4I; dppBz = 1,2-bis(diphenylphosphino)benzene) and [Au_2R_2(tpbz)] (R = C_6F_5, $C_6Cl_2F_3$, C_6Cl_5; tpbz = 1,2,4,5-tetrakis(diphenylphosphino)benzene).[11–13] As for mononuclear complexes, we investigated the origin of their TADF behaviour, which was attributed to metal–ligand ($AuPPh_2$) to ligand (C_6H_4) charge transfer (MLLCT) states that exhibit small $\Delta E(S_1–T_1)$ energy gaps. In these compounds, the variation of the perhalophenyl groups can modulate the electronic density of gold, and its SOC due to the presence of heavy atoms, such as iodine. The dppBz ligand, which contains two phosphorus centres that promote chelate coordination, gives rise to a rigid geometry that prevents non-radiative deactivation pathways. The TADF quantum yields obtained at room temperature are remarkably high – around 70% – although not spectacular.

For the dinuclear complexes, we adopted an alternative strategy inspired by the Davydov model,[14–17] which proposes that coupling between two transition dipole moments in a symmetric molecule yields two linear combinations. The antisymmetric (odd) combination, corresponding to antiparallel alignment, leads to a vanishing net transition moment, while the symmetric (even) combination results in a transition dipole moment approximately twice that of the monomer. By exploiting this effect, we achieved a four-fold enhancement in the radiative rate constant (k_r) relative to the mononuclear analogue. As a result, the TADF process becomes highly efficient at room temperature, with quantum yields exceeding 95%.

In summary, careful selection of the molecular structure leads to more efficient processes. Unfortunately, understanding the structural requirements necessary to achieve efficient TADF behaviour remains a key challenge. In this context, it is important to note that vibrational motion and non-radiative deactivation pathways are strongly affected by surrounding molecules, which may result from packing effects or even weak interactions with the emitter molecule. For this reason, computational studies provide valuable information.

A straightforward way to computationally account for environmental effects on the rigidity of molecular systems is the use of the ONIOM QM/MM approach. This method efficiently combines different levels of theory to model large molecular systems. A small part of the molecule, *i.e.* the emissive molecular system, is computed at a high quantum mechanical (QM) level of theory, while the surrounding molecular environment is computed at the molecular mechanics (MM) level of theory, permitting cost-effective computation with accurate results using, for example, the DFT level of theory. However, although modeling chemical structures using the ONIOM methodology is commonly used, excited state properties, as in full QM approaches, suffer from a large underestimation of the energy of charge-transfer states. Higher correlated methods such as ADC(2) are more appropriate for a more accurate description of the excited states involved in TADF processes. The environment is then considered using the ONIOM scheme. As far as we know, this approach has not been previously used in that context.

In this article, we investigate the influence of the structural characteristics of the acceptor group (a diphosphine) and the environment on the optical behaviour of gold compounds. Thus, complexes of stoichiometry [Au(diphosphine)$_2$][Au(C_6F_5)$_2$] (diphosphine = *cis*-1,2-bis(diphenylphosphino)ethylene (dppe), 1,2-bis(diphenylphosphino)benzene (dppBz), 4,5-bis(diphenylphosphino)-9,9-dimethylxanthene (Xantphos) and 1,8-bis(diphenylphosphino)naphthalene (dppn)) show different luminescent behavior depending on their intrinsic structural characteristics and their surrounding environment. The reasons for their different optical properties are explored through both experimental and computational approaches.

Results and discussion

Synthesis and characterization

The diphosphine-gold(I) complexes (**1–4**) have been synthesized by reacting the [Au(C_6F_5)(tht)] (tht = tetrahydrothiophene) gold(I) precursor with the dppe, dppBz, Xantphos or dppn ligands in equimolar ratios, using dichloromethane as solvent (Scheme 1). After 1 hour of stirring, evaporation of the solvent to *ca.* 1 mL and addition of *n*-hexane led to a precipitation of [AuL_2][Au(C_6F_5)$_2$] (L = dppe (**1**), dppBz (**2**), Xantphos (**3**), dppn (**4**)) as white (**1–3**) or orange (**4**) powders.

Analytical and spectroscopic data of the new complexes agree with the proposed stoichiometries, except for complex **1**, which crystallizes as a solvate with a formula [Au(dppe)$_2$][Au(C_6F_5)$_2$]·CH_2Cl_2 (**1**·CH_2Cl_2) (*vide infra*).

Their infrared spectra show absorption bands at ν = 782, 953, 1498 cm^{-1} (**1**); 779, 950, 1497 cm^{-1} (**2**); 780, 948, 1501 cm^{-1} (**3**); and 770, 951, 1499 cm^{-1} (**4**); associated with

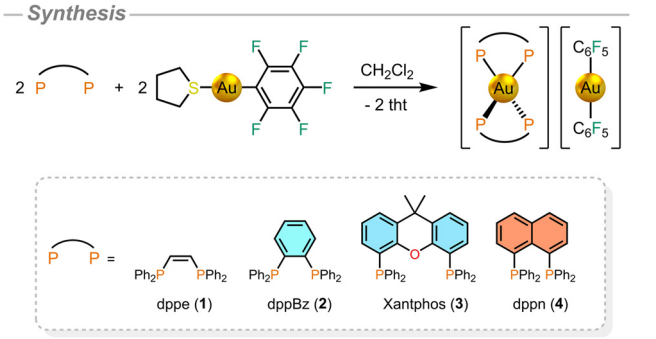

Scheme 1 Synthesis of **1–4** (tht = tetrahydrothiophene).

the anionic $[Au(C_6F_5)_2]^-$ fragments as well as bands related to the diphosphines (Fig. S1–S8).

The ^1H NMR spectra of the four complexes, measured in $CDCl_3$, display the aromatic protons of the ligands in the 7.11–7.35 (**1**), 7.03–7.52 (**2**), 6.59–7.48 (**3**) and 6.69–8.21 ppm (**4**) ranges. Complex **1** shows additional signals at 7.51 and 5.30 ppm, corresponding to the hydrogen atoms of the ethylene moiety and the dichloromethane molecules, respectively; while in **3**, the methyl groups on the xanthene fragment display a signal at 1.68 ppm (Fig. S9–S12).

The $[Au(C_6F_5)_2]^-$ counterion is as well confirmed through $^{19}F\{^1H\}$ NMR measurements showing the three characteristic signals for the fluorine atoms in *ortho*, *meta* and *para* positions (Fig. S19–S22).[18]

The $^{31}P\{^1H\}$ spectra (Fig. S23–S26), show singlets at 22.50 (**1**), 21.19 (**2**), 4.69 (**3**) and 7.58 ppm (**4**), indicating that the phosphorous atoms are identical at RT.

Crystal structures

The crystal structures of **1**·CH_2Cl_2, **2** and **4** were determined by X-ray diffraction studies of single crystals obtained by slow diffusion of *n*-hexane to saturated dichloromethane solutions. Complex **1** crystallizes in the $P\bar{1}$ space group of the triclinic system, with one dichloromethane molecule per compound molecule, while **2** and **4** crystallize in the $C2/c$ space group of the monoclinic system (Table S2). Although suitable crystals of **3** could not be obtained, the structure of the cationic $[Au(Xantphos)_2]^+$ moiety with a similar counterion ($[Au(Xantphos)_2][Au(C_6Cl_2F_3)_2]$) (**3***) has previously been reported by us,[19] and will here be used for comparison purposes.

The three structures show similarities and can be described as formed by two ionic fragments, resulting from a reorganization of the ligands during the crystallization process favoured by the high polarity of the solvent (dichloromethane). The atoms in the anionic $[Au(C_6F_5)_2]^-$ moieties adopt a nearly linear environment in **3*** and **4** with C–Au–C angles of 173.6(4)° and 176.1(3)°, respectively, while in **1**·CH_2Cl_2 and **2** they exhibit a perfectly linear arrangement (Fig. 1, top), since these metal centres are located in special positions and the entire $[Au(C_6F_5)_2]^-$ fragment is generated by symmetry. Therefore, the perhaloaryl groups in **1**·CH_2Cl_2 and **2** are parallel, while in **3*** and **4**, they are slightly rotated by torsion angles of 29.4° and 26.5°, respectively.

The coordinated diphosphine ligands in the cationic $[Au(diphosphine)_2]^+$ moieties are not very distorted from the structure of their free form.[20–25] The gold atoms within the cationic complexes display a pseudo-tetrahedral geometry with intraligand P–Au–P angles of 86.33(3) and 86.98(3)° for dppe in **1**·CH_2Cl_2, 84.62(4)° for the dppBz ligands in **2**, 108.1(1) and 108.9(1)° for Xantphos in **3***, and 86.47(4) and 85.71(4)° for dppn in **4** (Fig. 1, bottom). The cations containing dppe, dppBz or dppn as ligands display narrower bite angles, which

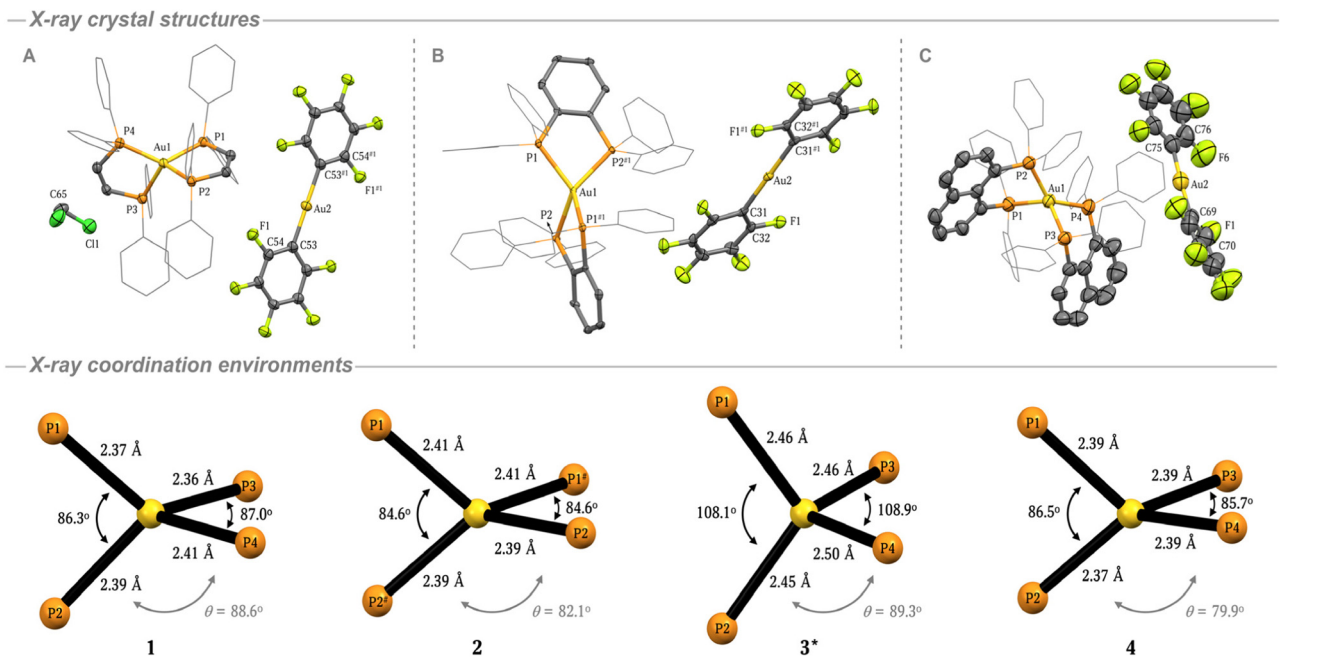

Fig. 1 Top: The molecular structure of **1**·CH_2Cl_2 (A), **2** (B) and **4** (C) (50% probability ellipsoids) with the labelling scheme adopted for the atom positions. Selected bond lengths (Å) and angles (°): Au1–P1 2.3727(9), Au1–P2 2.3854(9), Au1–P3 2.3600(9), Au1–P4 2.4093(9), Au2–C53 2.054(4), Au2–C59 2.044(3), P1–Au1–P2 86.33(3), P3–Au1–P4 86.98(3), P1–Au1–P3 129.36(3), P1–Au1–P4 115.14(3), P2–Au1–P3 126.05(3), P2–Au1–P4 115.69(3), C–Au2–C 180.0 (**1**·CH_2Cl_2); Au1–P1 2.4053(12), Au1–P2 2.3942(12), Au2–C31 2.043(5), P1–Au1–P2# 84.62(4), P1–Au1–P2 118.83(4), P1–Au1–P1# 124.17(6), P2–Au1–P2# 130.98(6), C–Au2–C 180.0 (**2**); and Au1–P1 2.3932(11), Au1–P2 2.3718(11), Au1–P3 2.3846(12), Au1–P4 2.3855(13), Au2–C69 2.039(7), Au2–C75 2.042(7), P1–Au1–P2 86.47(4), P3–Au1–P4 85.71(4), P1–Au1–P3 121.60(4), P1–Au1–P4 115.39(4), P2–Au1–P3 117.12(4), P2–Au1–P4 134.89(4), C–Au2–C 176.1(13) (**4**). Hydrogen atoms have been omitted for clarity. Symmetry transformations are used to generate equivalent atoms in **2**. # $-x+1, y, -z+\frac{1}{2}$. Bottom: The coordination of the gold(I) centres of **1**·CH_2Cl_2 (left), **2** (centre-left), **3*** (centre-right) and **4** (right).

is due to the structural restrictions caused by the C=C bonds connecting the phosphorus atoms. In contrast, the diphosphine Xantphos can adopt a boat-like conformation by folding its xanthene fragment along the $CMe_2\cdots O$ axis, leading to wider bite angles. Obviously, the narrower the P–Au–P intraligand angle is, the wider is the interligand one. The environment of the gold atom in the cationic complexes is defined not only by the diphosphine angles, but also by the Au–P distances, which range from 2.3600(9) to 2.4093(9) Å in the structures of **1**·CH_2Cl_2, **2** and **4**, containing rigid diphosphines, while **3***, containing the more flexible Xantphos ligand, displays longer Au–P distances that vary from 2.452(3) to 2.497(4) Å. Therefore, it is possible to establish a relationship between the diphosphine bite angle, and the distortion of the coordination sphere.

The dihedral angles between the planes defined by the intraligand P–Au–P angles are 88.6 (**1**·CH_2Cl_2), 82.1 (**2**), 89.3 (**3***) and 79.9° (**4**) (Fig. 1, bottom). Although Xantphos is more flexible because it can adopt the boat-like conformation, the dihedral angle in **1**·CH_2Cl_2 is very close to that in **3***.

Photophysical properties at room temperature and at 77 K

The absorption spectra in the solid state of **1–4** show bands between 200 and 350–500 nm, which are also observed in measurements of the absorption spectra of the diphosphine ligands and the $[Au(C_6F_5)_2]^-$ anion (Fig. S27–S30; S31–S34 display the absorption spectra in solution). The high-energy bands can be assigned to $\pi \rightarrow \pi^*$ or $\sigma \rightarrow \pi^*$ intra-ligand transitions of the diphosphine ligands, or the perhalophenyl rings, and charge-transfer transitions of the perhalophenyl rings and the metal centre of the counterion.

The absorption bands between 330 and 500 nm have edges at lower energies than for the precursors, which may be due to charge-transfer processes between the gold(I) centre and the diphosphine ligands.

The studied complexes, except $[Au(dppe)_2][Au(C_6F_5)_2]$ (**1**), have strong emission when irradiated with UV-vis light (Fig. 2). At RT, **2** and **3** have an emission band at 491 nm with quantum yields (Φ) of 0.60 (**2**), 0.21 (**3**), respectively, when excited in the 250–400 nm range, whereas **4** exhibits an emission band centred at 686 nm (Φ = 0.59) when it is excited in the 250–600 nm range. The shift in the emission wavelength of **4** is probably due to the presence of fused aromatic rings in the phosphine ligands that reduces the HOMO–LUMO gap and therefore shifts the emission to lower energies.[26] The emission lifetimes are 3.3 (**2**), 3.1 (**3**) and 7.8 μs (**4**) at RT.

The emission bands at 77 K are somewhat shifted towards the blue with maxima at 487 (**2**), 483 (**3**) and 704 nm (**4**). The lifetimes are significantly longer than at RT, with values of 19.4 (**2**), 11.7 (**3**) and 23.8 μs (**4**).

The shorter emission lifetimes at RT and the small shift of the emission bands when cooling the samples suggest TADF emission at RT as previously discussed for other diphosphinogold(I) complexes.[11,12]

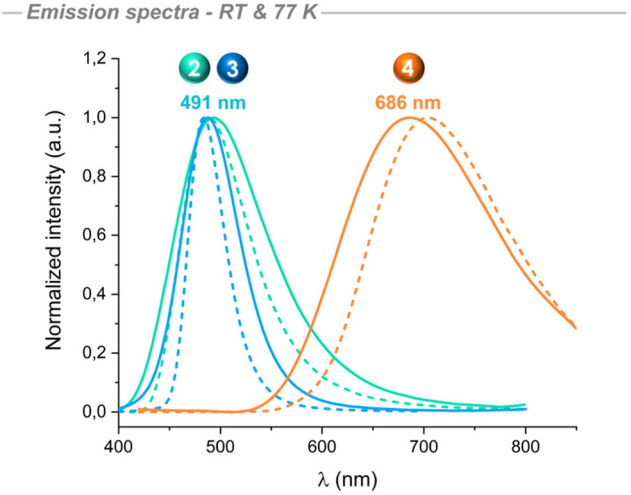

Fig. 2 Experimental emission spectra in the solid state of $[Au(dppBz)_2][Au(C_6F_5)_2]$ (**2**) (turquoise), $[Au(Xantphos)_2][Au(C_6F_5)_2]$ (**3**) (blue) and $[Au(dppn)_2][Au(C_6F_5)_2]$ (**4**) (orange) measured at RT (solid) and at 77 K (dashed).

Thermally activated delayed fluorescence studies

The solid-state emission lifetimes were measured in the temperature range of 77–348 K for **2** and **3** and 77–378 K for **4** showing that the lifetime decreases with increasing temperature. The emission lifetimes as a function of the temperature were fitted to a Boltzmann-type function:[27,28]

$$\tau_{av} = \frac{3 + \exp(-\Delta E(S_1 - T_1)/k_B T)}{3/\tau_T + 1/\tau_S \exp(-\Delta E(S_1 - T_1)/k_B T)} \quad (2)$$

where k_B is Boltzmann's constant, and τ_T and τ_S are the lifetimes of the phosphorescence ($T_1 \rightarrow S_0$) and the prompt fluorescence ($S_1 \rightarrow S_0$), respectively. The energy difference ($\Delta E(S_1$–$T_1)$) and the lifetime of the fluorescence were obtained by fitting eqn (2) to the measured emission decay times using τ_T values of 19.4 (**2**), 11.7 (**3**) and 23.8 μs (**4**), which were measured at 77 K, which is assumed to be due to pure phosphorescence (Fig. 3, top, and Fig. S41–S43, SI).

The fit yielded $\Delta E(S_1$–$T_1)$ values of 592 (**2**), 925 (**3**) and 562 cm^{-1} (**4**). The smallest $\Delta E(S_1$–$T_1)$ is obtained for **4** with the naphthalene ring of the dppn ligand. Complex **2**, with a phenylene ring of the dppBz ligand, has almost the same $\Delta E(S_1$–$T_1)$ gap as **4**, whereas a much larger $\Delta E(S_1$–$T_1)$ is obtained for **3**.

The emission lifetime of **2** is almost constant ($\tau \approx 19$ μs) between 77 and 100 K, which can be assigned to the pure $T_1 \rightarrow S_0$ phosphorescence process. Increasing the temperature leads to a decrease in the lifetime due to the fluorescence from the energetically higher lying S_1 state. The emission rate increases with temperature until TADF dominates the emission, reaching an almost constant lifetime at 338 K ($\tau_{338\ K} \approx 2$ μs). A constant emission due to phosphorescence is also observed for $[Au(Xantphos)_2][Au(C_6F_5)_2]$ (**3**) between 77 and 180 K, with $\tau \approx$ 12 μs (Fig. 3, top). The TADF process begins at higher temperatures, reaching a constant lifetime of $\tau_{338\ K} \approx 2$ μs at 338 K.

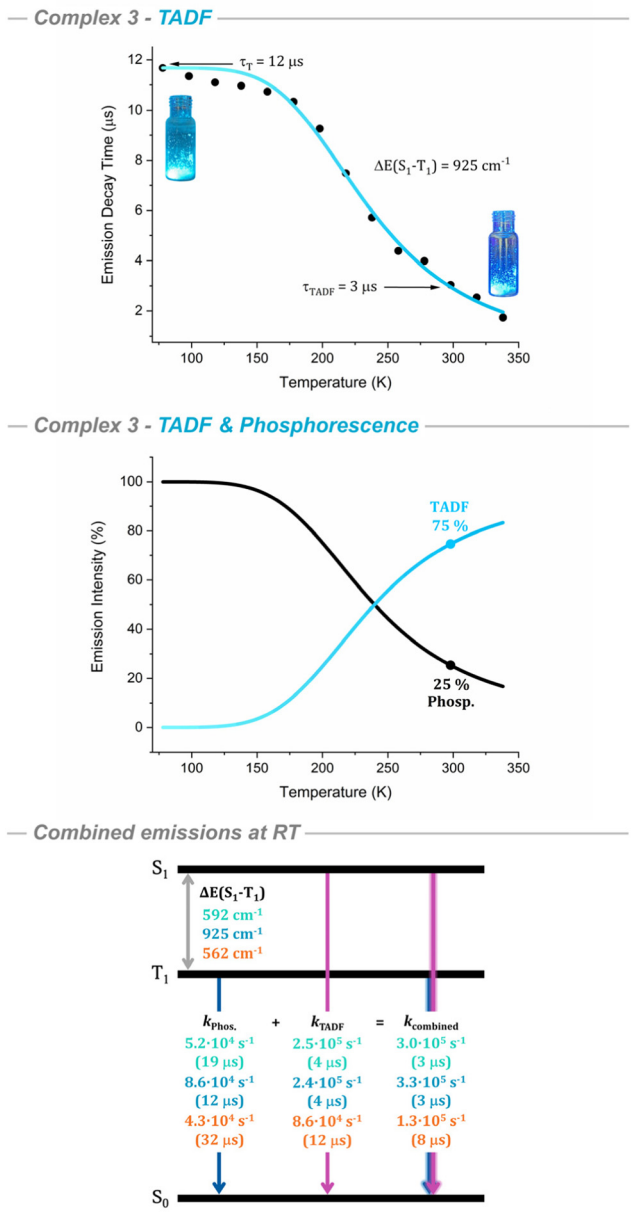

Fig. 3 Top: The emission decay times of complex **3** *versus* temperature. The solid line represents a fit of the experimental data to a Boltzmann-type expression. Middle: Relative emission intensities of **3** from TADF and direct phosphorescence as a function of temperature calculated from experimental data using eqn (4) and (5). Bottom: Schematic energy level diagram and decay times of **2** (turquoise), **3** (blue) and **4** (orange).

The TADF lifetime for $[Au(dppn)_2][Au(C_6F_5)_2]$ (**4**) is almost constant at 378 K yielding $\tau_{378\ K} \approx 4$ µs. However, a plateau at low temperature is not observed as for **2** and **3**, suggesting that TADF occurs even at 77 K.

When the populations of S_1 and T_1 follow the Boltzmann distribution, the relative contribution to the emission intensity of phosphorescence and TADF at a given temperature is given by:[29]

$$\frac{I(T_1)}{I_{tot}} = \left[1 + \frac{k_r(S_1)g(S_1)}{k_r(T_1)g(T_1)} e^{-\Delta E(S_1-T_1)/k_B T}\right]^{-1} \quad (3)$$

where the $k_r(S_1)$ and radiative constants can be expressed as a function of the quantum yield (Φ) and the emission decay time (τ). The radiative rate constant is given by $k_r = \Phi\tau^{-1}$, $g(S_1) = 1$ and $g(T_1) = 3$ are the degeneracy factors of the singlet and triplet states, respectively. I_{tot} is the total emission intensity of the singlet and triplet states.

eqn (3) can be simplified when assuming that photoluminescence quantum yields for the phosphorescence and TADF processes are the same ($\Phi(S_1) = \Phi(T_1)$):[30,31]

$$\frac{I(T_1)}{I_{tot}} = \left[1 + \frac{\tau(T_1)}{3\tau(S_1)} e^{-\Delta E(S_1-T_1)/k_B T}\right]^{-1} \quad (4)$$

Using $I_{tot} = I(S_1) + I(T_1)$ we obtain

$$\frac{I(S_1)}{I_{tot}} = 1 - \left[1 + \frac{\tau(T_1)}{3\tau(S_1)} e^{-\Delta E(S_1-T_1)/k_B T}\right]^{-1} \quad (5)$$

The temperature dependent ratio between the TADF and phosphorescence intensities can be calculated by inserting the emission parameters $\Delta E(S_1–T_1)$ = 592 (**2**), 925 (**3**), 562 cm^{-1} (**4**); $\tau(S_1)$ = 69 (**2**), 15 (**3**), 247 ns (**4**); $\tau(T_1)$ = 19 (**2**), 12 (**3**), 24 µs (**4**) into eqn (4) and (5). In Fig. 3 (middle) and Fig. S44–S46 (SI), one sees that the $S_1 \rightarrow S_0$ TADF intensities reach values of 84% (**2**), 75% (**3**) and 67% (**4**) at RT.

Due to the fast equilibrium between the S_1 and T_1 states, only the averaged emission decay time from the $S_1 \rightarrow S_0$ and $T_1 \rightarrow S_0$ transitions is experimentally accessible. Although the contribution from T_1 to the total emission intensity decreases as the temperature increases, it still contributes at RT.

The TADF and phosphorescence rate constants at RT can be estimated by comparing the rate constants of the individual processes using eqn (6):[30,32,33]

$$k(\text{combined}) = k(\text{TADF}) + k(T_1), \quad (6)$$

with k(combined) = k(298 K) = 3.04×10^5 (**2**), 3.28×10^5 (**3**), 1.29×10^5 s^{-1} (**4**) and using $k(T_1) = 5.16 \times 10^4$ (**2**), 8.57×10^4 (**3**), 4.26×10^4 s^{-1} (**4**), we obtain k(TADF) = 2.52×10^5 (**2**), 2.43×10^5 (**3**) and 8.62×10^4 s^{-1} (**4**) (Fig. 3, bottom).

Computational studies

We optimized the molecular structures of the S_0, S_1 and T_1 states of **2**, **3** and **4** in the gas phase[34–37] at the DFT level (models **2a–4a**). Excitation energies, spin–orbit coupling (SOC) matrix elements and rate constants were calculated using the optimized structures of the S_1 state (Table S4). It is unlikely that the molecules in the gas phase emit *via* the TADF mechanism because the calculated $\Delta E(S_1–T_1)$ of 1899 (**2a**), 4498 (**3a**) and 3836 cm^{-1} (**4a**) are much larger than the typical TADF energy threshold of about 1000 cm^{-1}.[38–40] Gas-phase calculations cannot properly describe the luminescence properties of the studied molecules in the solid state implying one must use a more sophisticated computational approach. We designed a two-layer QM/MM ONIOM scheme that considers environmental effects, which we applied to clusters constructed from the crystal unit cell (models **2b–4b**) and then

some of the molecules or fragments at the cluster boundaries were removed.[41–46]

Comparison of the excitation energies calculated for **2** using various cluster sizes showed that the cluster built from the 1 × 1 × 2 supercell (**2b**) (Fig. 4, top), consisting of the central emitter and 16 surrounding molecules for **2**, is a good compromise between computational costs and the accuracy of the obtained results (Table S5). The cluster model was also used for studying **3** and **4**, with 23 and 30 surrounding molecules respectively, which were constructed from supercells with dimensions 2 × 2 × 2 (**3b** and **4b**, respectively) (Fig. S47–S49). In the time-dependent DFT (TDDFT) calculations on the ONIOM-based models (Table S6), the excitation energy of the T_1 state calculated using the molecular structure of the S_1 state is much larger than the excitation energies of the T_1 state calculated in the gas phase. The $\Delta E(S_1–T_1)$ splitting in the ONIOM calculations at the TDDFT level are 1214 (**2b**), 2112 (**3b**) and 2184 cm^{-1} (**4b**), which are closer to the TADF threshold, but still larger than the experimental values. In the TDDFT calculations on the ONIOM-based models, the T_2 state of the three molecules is energetically above the S_1 state, which is not the case in the gas-phase calculations. The environmental effect increases the energy of the S_0–S_1 transition of **2** from 9505 cm^{-1} in the gas phase (**2a**) to 21473 cm^{-1} in the crystal (**2b**) (Tables S4 and S6), which is in good agreement with the experimental value of 20367 cm^{-1} (λ_{em} = 491 nm). The calculations show that it is necessary to consider environmental effects for a proper description of the excited states. However, the S_1–T_1 gap is still too large for TADF at the TDDFT level.

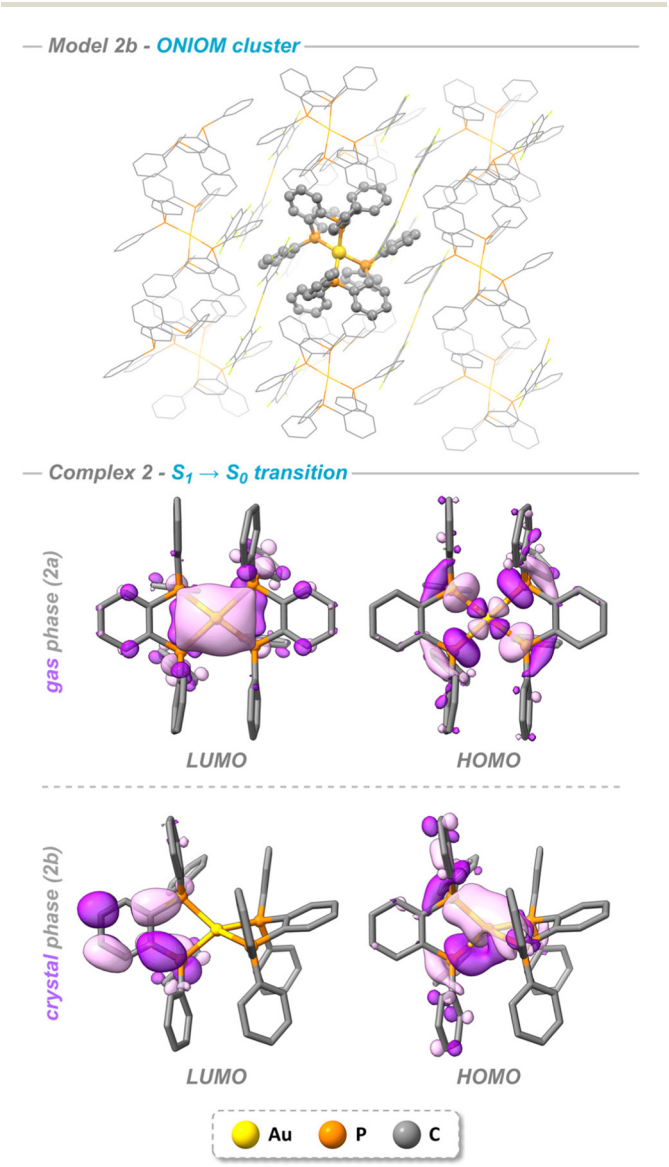

Fig. 4 Top: Cluster constructed from the unit cell with dimensions 1 × 1 × 2 illustrating the position of **2** in the crystal environment. The region treated at the TDDFT level is shown in the ball and stick representation, while the region treated with xTB is shown as lines to highlight the spatial arrangement and packing effects. Bottom: Representation of the optimized molecular structures of **2** in the S_1 gas-and crystal-phase states along with their corresponding frontier molecular orbitals (HOMO and LUMO, isovalue = 0.03). Hydrogen atoms have been omitted for clarity.

The molecular structure of the S_1 state of model **2b** (Fig. S48) is closer to the structure of the S_0 state of model **2a** than the structure of the S_1 state of model **2a** (Table S7). The crystal environment prevents significant distortions of the molecular structure of the excited state, whereas in the absence of the molecular environment the molecular structure of the S_1 state relaxes to an almost planar coordination of the gold(I) centre, leading to a very small excitation energy.

The molecular structures of the S_1 state of models **2b**, **3b**, and **4b** are very similar to the ground-state structures of models **2a–4a** (Fig. S50–S52 and Tables S7–S9). The Au–P bond lengths of the S_1 state are 2.43–2.55 (**2b**), 2.48–2.53 (**3b**) and 2.38–2.42 Å (**4b**) as compared to those of the S_0 state of 2.42 (**2a**), 2.50–2.53 (**3a**) and 2.39–2.40 Å (**4a**) and to the experimental values 2.39–2.41 (**2**), 2.45–2.50 (**3***) and 2.37–2.39 Å (**4**).

The intraligand P–Au–P angles of **2** and **4** change slightly from 86.23° (**2a**), 85.73 and 85.38° (**4a**) in the S_0 state to 80.81 and 81.48° (**2b**), 85.13 and 85.08° (**4b**) in the S_1 state. However, the main distortions arise from a twist in the dihedral interligand angles ($\theta_{P–Au–P}$), which decrease from 85.48 (**2a**) and 79.58° (**4a**) in the S_0 state to 72.92 (**2b**) and 70.15° (**4b**) in the S_1 state (Tables S7 and S9).

The structural relaxation of the excited state of **3** differs from that of **2** and **4**. The intra- and interligand P–Au–P angles in **3** change significantly upon excitation to the S_1 state, while the dihedral interligand angle increases by only one degree (Table S8). The structural distortions are located in the xanthene moieties, which adopt a more pronounced boat-like conformation in the S_1 state, leading to a widening of the angles from 141.37 and 146.35° in S_0 (**3a**) to 155.44 and 149.39° in S_1 (**3b**).

The dppBz and dppn ligands in **2** and **4** lead to a closer structural similarity between the S_0 and S_1 states in the solid state. The structural rigidity is more pronounced for dppn, while Xantphos allows a greater structural distortion in **3**. The structural rigidity increases in the following order: Xantphos

(**3**) < dppBz (**2**) < dppn (**4**), which is directly reflected in the experimental S_1–T_1 energy gaps of 925 (**3**) > 592 (**2**) > 562 cm^{-1} (**4**). A more flexible environment leads to larger structural distortions of the excited states and to a larger energy difference between them.

In the ONIOM calculations on **2b**, the $S_1 \rightarrow S_0$ transition leads to charge transfer from the phenylene group on the dppBz ligand to the gold centre and the phosphorus atoms, which is necessary for TADF. This charge transfer character was further confirmed by transition density analyses, which clearly show the flow of electron density from the ligand to the metal centre (Fig. S53). In the gas-phase calculations, there is almost no charge transfer because the HOMO and the LUMO orbitals are localized on the gold centre (Fig. 4, bottom).

Although the optimized molecular and electronic structure calculations in the solid state agree better with experimental data than those performed in the gas phase, the computed $\Delta E(S_1–T_1)$ values still exceed 1000 cm^{-1}, which is larger than the experimental values (Table S6), and inconsistent with emission *via* the TADF mechanism.

Excitation energies calculated at the TDDFT level in the gas phase, from the molecular structure optimized for the S_1 state using the ONIOM approach (models **2b***–**4b***), are close to those obtained when explicitly considering the environment through the ONIOM model. The largest difference is obtained for **4**, which has a deviation of 1414 cm^{-1} between the gas-phase excitation energy of 18509 cm^{-1} (**4b***) (Table 1) and the one of 17094 cm^{-1} obtained for the S_1 state using the ONIOM approach (**4b**) (Table S6). The small difference arises from the polarization of the electron density by the crystal environment. Accurate excitation energies can be obtained by performing calculations at *ab initio* correlated level of theory using the molecular structure optimized with the ONIOM model.

We have employed the ADC(2) method that describes singlet and triplet excited states with high accuracy and can be applied to large molecules, improving the TDDFT/ONIOM description of the TADF process (models **2c–4c**) (see Table 1).[47,48] Calculations of the excitation energies, $k_{ISC}(S_1 \rightarrow T_1)$ and $k_{RISC}(T_1 \rightarrow S_1)$ were performed as the single-point calculations at the ADC(2) level using the molecular structure of the S_1 state optimized at TDDFT/ONIOM level of theory, whereas the SOC matrix elements were calculated at the TDDFT level.

The ADC(2) calculations yielded larger excitation energies of the T_1 state energies than at the TDDFT level resulting in a smaller energy difference of 567 (**2c**), 1196 (**3c**) and 848 cm^{-1} (**4c**) between the S_1 and T_1 states. The energy gaps calculated at the ADC(2) level are much closer to the experimental values of 592 (**2**), 925 (**3**) and 562 cm^{-1} (**4**).

The prompt fluorescence lifetimes (τ_S) were calculated using $k_r(S_1 \rightarrow S_0)$ and the Strickler–Berg formula.[49] The excitation energies and oscillator strengths were calculated at the ADC(2) level in the gas phase using the molecular structure of S_1 optimized at the TDDFT/ONIOM level. The obtained τ_S of 0.13 (**2c**), 0.22 (**3c**), and 0.13 μs (**4c**) agree well with the experimental values of 0.07 (**2**), 0.02 (**3**), and 0.25 μs (**4**) (Table 1). TDDFT calculations using a supercell model, yielded τ_S values of 0.12 (**2b***), 0.21 (**3b***), and 0.09 μs (**4b***) (Table S6). Lifetime calculations using the molecular structure of the S_1 state optimized in the gas phase yielded for **2a** a τ_S value of 20.75 μs, which is more than two orders of magnitude larger than the experimental value, whereas for **3a** and **4a**, the corresponding τ_S values agree within one order of magnitude with experimental values (Table S4).

The calculated photoluminescence quantum yields (Φ) of 0.85 (**2c**), 0.95 (**3c**), and 0.70 (**4c**) are larger than the experimental values of 0.60, 0.21, and 0.59, respectively, probably because intermolecular quenching is neglected in the calculations.

The ADC(2) calculations yielded rate constants for $k_{ISC}(S_1 \rightarrow T_1)$ of 2.9×10^{12} (**2c**), 4.3×10^{12} (**3c**) and 6.7×10^{12} s^{-1} (**4c**), and for $k_{RISC}(T_1 \rightarrow S_1)$ at RT is 1.9×10^{11} (**2c**), 1.4×10^{10} (**3c**) and 1.1×10^{11} s^{-1} (**4c**), which are several orders of magnitude larger than k_r of the $S_1 \rightarrow S_0$ transition (Table 1). The calculated spin–orbit coupling matrix elements $(S_1|H_{SO}|T_1)$ are 64 (**2b***), 100 (**3b***) and 108 cm^{-1} (**4b***). Calculations at the ADC(2) level do not underestimate the excitation energies between the S_1 and T_1 states and the ground state, as in previous studies at other levels of theory.[11,12] Including the molecular environment at the TDDFT/ONIOM level prevents large structural distortions, leading to reliable optimized structures of the excited states. The $(S_1|H_{SO}|T_1)$ values indicate a strong SOC effect in the excited electronic states, which leads to large k_{ISC} and k_{RISC} values that promotes a fast transfer between T_1 and S_1, which is fundamental for TADF.

Table 1 Excitation energies (cm^{-1}), oscillator strengths (f), and spin–orbit coupling (SOC) matrix elements $(S_1|H_{SO}|T_1)$ (cm^{-1}) for **2b***, **3b***, and **4b*** calculated at the TDDFT level. Excitation energies calculated for **2c**, **3c** and **4c** at the ADC(2) level are also reported. The rate constants and fluorescence lifetime (τ_S) are estimated based on the ADC(2) excitation energies. The calculations were carried out in the gas phase using the optimized molecular structure of the S_1 state obtained in the two-layer ONIOM calculation. Experimental values are given in parenthesis

Level		2	3	4
TDDFT	S_1	22 369.8	26 893.7	18 508.8
	T_1	21 092.2	23 727.2	14 488.9
	T_2	24 174.0	25 890.4	18 629.0
	$\Delta E(S_1–T_1)$	1277.6	3166.5	4019.9
ADC(2)	S_1	23 658.9	26 040.8	16 562.8
	T_1	23 091.5	24 844.6	15 714.9
	T_2	27 205.8	28 682.6	19 797.8
	$\Delta E(S_1–T_1)$	567.3	1196.2	848.0
	$f(S_1)$	0.0208	0.0099	0.0426
	$(S_1\|H_{SO}\|T_1)$	63.73	100.29	107.96
	τ_S	0.13 (0.07)	0.22 (0.02)	0.13 (0.25)
	$k_r(S_1 \rightarrow S_0)$	7.8×10^6	4.5×10^6	7.8×10^6
	$k_{IC}(S_1 \rightarrow S_0)$	1.4×10^6	2.2×10^5	4.4×10^6
	$k_{ISC}(S_1 \rightarrow T_1)$	2.9×10^{12}	4.3×10^{12}	6.7×10^{12}
	$k_{RISC}(T_1 \rightarrow S_1)$	1.9×10^{11}	1.4×10^{10}	1.1×10^{11}
	Φ	0.85 (0.60)	0.95 (0.21)	0.70 (0.59)

Experimental

General considerations

The starting precursor [Au(C_6F_5)(tht)] was prepared as described in the literature.[50,51] The dppe, dppBz and Xantphos ligands were purchased from Sigma-Aldrich, whereas dppn was obtained from BLDpharm; all of them were used as received. All solvents used for the synthesis of the new compounds were obtained from commercial sources and were employed without further purification.

Instrumentation

The infrared spectra were recorded in the 2000–450 cm^{-1} range using a PerkinElmer FT-IR Spectrum Two with an ATR accessory. The C and H analyses were carried out with a PerkinElmer 240C microanalyzer. The ESI-MS spectra were obtained using a Esquire3000 plus spectrometer equipped with an API-ESI source and a QToF mass analyser (**1**, **2**) and using a Bruker MicroTOF-Q spectrometer with an ESI ionization source (**3**, **4**). The $^{31}P\{^1H\}$, $^{19}F\{^1H\}$, $^{13}C\{^1H\}$ and ^1H NMR experiments were recorded in $CDCl_3$ using a Bruker ARX 300 and a Bruker AVANCE 400. Chemical shifts are reported relative to H_3PO_4 (^{31}P, external), $CFCl_3$ (^{19}F, external) and $SiMe_4$ (^1H and $^{13}C\{^1H\}$ external). Diffuse reflectance UV-vis spectra of pressed powder samples diluted with KBr were recorded on a Shimadzu UV-3600 spectrophotometer with a Harrick Praying Mantis accessory and recalculated following the Kubelka–Munk function. Excitation and emission spectra in the solid state as well as lifetime measurements were recorded using an Edinburgh FLS 1000 fluorescence spectrometer. The quantum yields were measured in the solid state using a Hamamatsu Quantaurus-QY C11347-11 integrating sphere with excitations at 330 (**2**), 280 (**3**) and 450 nm (**4**).

Synthesis and characterization

[AuL_2][Au(C_6F_5)$_2$] (L = dppe (**1**), dppBz (**2**), Xantphos (**3**), dppn (**4**)) were synthesized by adding the [Au(C_6F_5)(tht)] gold precursor (0.100 g, 0.221 mmol) in a 1 : 1 molar ratio to a dichloromethane solution (20 mL) of the corresponding diphosphine ligand dppe (0.088 g, 0.221 mmol) (**1**), dppBz (0.098 g, 0.221 mmol) (**2**), Xantphos (0.128 g, 0.221 mmol) (**3**) or dppn (0.110 g, 0.221 mmol) (**4**). After 1 hour of stirring at room temperature, the solvent was evaporated under vacuum to *ca.* 1 mL. Finally, addition of *n*-hexane (20 mL) induced the precipitation of products **1** (0.109 g, 65%), **2** (0.151 g, 84%) or **3** (0.184 g, 88%) as white solids, and of product **4** (0.146 g, 77%) as an orange one. The synthesis of **4** was performed under inert atmosphere conditions using anhydrous solvents, due to the high sensitivity of the dppn ligand to oxidation in the presence of oxygen or moisture.

Experimental data for 1. Anal. (%) calcd for **1** ($C_{65}H_{46}Au_2Cl_2F_{10}P_4$): C, 48.62; H, 2.89. Found: C, 50.71; H, 2.98. ^1H NMR (298 K, $CDCl_3$): δ 7.51 (m, 4H, Et), δ 7.35 (t, 16H, H_o, PPh_2, $^3J_{H-H}$ = 8 Hz), δ 7.16 (t, 8H, H_p, PPh_2, $^3J_{H-H}$ = 8 Hz), δ 7.11 (m, 16H, H_m, PPh_2), δ 5.30 (s, 2H, CH_2Cl_2). $^{19}F\{^1H\}$ NMR (298 K, $CDCl_3$): δ −114.80 (m, 4F, F_o), δ −162.68 (t, 2F, F_p), δ −163.99 (m, 4F, F_m). $^{31}P\{^1H\}$ NMR (298 K, $CDCl_3$): δ 22.50 (s, 4P). MS, ESI(−): *m*/*z* 530.95 [Au(C_6F_5)$_2$]$^-$. ESI(+): *m*/*z* 989.21 [Au(dppe)$_2$]$^+$. ATR-IR: ν 782, 953, 1498 cm^{-1} [Au(C_6F_5)$_2$]$^-$; ν 691, 730, 1434, 1484 cm^{-1} (dppe).

Experimental data for 2. Anal. (%) calcd for **2** ($C_{72}H_{48}Au_2F_{10}P_4$): C, 53.35; H, 2.98. Found: C, 53.52; H, 3.11. ^1H NMR (298 K, $CDCl_3$): δ 7.52 (m, 4H, C_6H_4), δ 7.46 (m, 4H, C_6H_4), δ 7.31 (t, 16H, H_m, PPh_2, $^3J_{H-H}$ = 8 Hz), δ 7.08 (t, 8H, H_m, PPh_2, $^3J_{H-H}$ = 8 Hz), δ 7.03 (m, 16H, H_o, PPh_2). $^{19}F\{^1H\}$ NMR (298 K, $CDCl_3$): δ −114.93 (m, 4F, F_o), δ −162.88 (t, 2F, F_p), δ −164.18 (m, 4F, F_m). $^{31}P\{^1H\}$ NMR (298 K, $CDCl_3$): δ 21.19 (s, 4P). MS, ESI(−): *m*/*z* 530.95 [Au(C_6F_5)$_2$]$^-$. ESI(+): *m*/*z* 1089.24 [Au(dppBz)$_2$]$^+$. ATR-IR: ν 779, 950, 1497 cm^{-1} [Au(C_6F_5)$_2$]$^-$; ν 691, 741, 1434, 1482 cm^{-1} (dppBz).

Experimental data for 3. Anal. (%) calcd for **3** ($C_{90}H_{64}Au_2F_{10}O_2P_4$): C, 57.34; H, 3.42. Found: C, 57.32; H, 3.53. ^1H NMR (298 K, $CDCl_3$): δ 7.48 (m, 4H, xanthene), δ 7.18 (m, 20H, xanthene and H_m in PPh_2), δ 7.05 (t, 8H, H_p, PPh_2, $^3J_{H-H}$ = 8 Hz), δ 6.84 (m, 16H, H_o, PPh_2), δ 6.59 (m, 4H, xanthene), δ 1.68 (s, 12H, CH_3). $^{19}F\{^1H\}$ NMR (298 K, $CDCl_3$): δ −114.73 (m, 4F, F_o), δ −160.93 (t, 2F, F_p), δ −163.08 (m, 4F, F_m). $^{31}P\{^1H\}$ NMR (298 K, $CDCl_3$): δ 4.69 (br, 4P). MS, ESI(−): *m*/*z* 530.94 [Au(C_6F_5)$_2$]$^-$. ESI(+): *m*/*z* 1353.35 [Au(Xantphos)$_2$]$^+$. ATR-IR: ν 780, 948, 1501 cm^{-1} [Au(C_6F_5)$_2$]$^-$; ν 692, 741, 1227, 1406, 1434 cm^{-1} (Xantphos).

Experimental data for 4. Anal. (%) calcd for **4** ($C_{80}H_{52}Au_2F_{10}P_4$): C, 55.83; H, 3.05. Found: C, 55.40; H, 3.08. ^1H NMR (298 K, $CDCl_3$): δ 8.21 (m, 4H, naphthalene), δ 7.54 (m, 4H, naphthalene), δ 7.10 (m, 20H, xanthene and H_m in PPh_2), δ 6.79 (t, 8H, H_p, PPh_2, $^3J_{H-H}$ = 8 Hz), δ 6.69 (m, 16H, H_o, PPh_2). $^{19}F\{^1H\}$ NMR (298 K, $CDCl_3$): δ −114.88 (m, 4F, F_o), δ −162.95 (t, 2F, F_p), δ −164.16 (m, 4F, F_m). $^{31}P\{^1H\}$ NMR (298 K, $CDCl_3$): δ 7.58 (s, 4P). MS, ESI(−): *m*/*z* 530.98 [Au(C_6F_5)$_2$]$^-$. ESI(+): *m*/*z* 1189.26 [Au(dppn)$_2$]$^+$. ATR-IR: ν 770, 951, 1499 cm^{-1} [Au(C_6F_5)$_2$]$^-$; ν 690, 742, 1434, 1478 cm^{-1} (dppn).

Computational details

The initial gas-phase calculations performed using TDDFT are referred to as models **2a–4a**. The subsequent ONIOM-based models, in which the central molecules are treated at the TDDFT level, are denoted as **2b–4b**. When the geometries optimized within these ONIOM models are used for further gas-phase calculations, still employing TDDFT, the resulting models are referred to as **2b*–4b***. When the same geometries are used for gas-phase calculations at the ADC(2) level of theory, the corresponding models are denoted as **2c–4c**.

The molecular structures of the ground state (S_0), and of the first excited singlet state (S_1) of **2**, **3**, and **4** were optimized in the gas phase. The optimizations were performed at the density functional theory (DFT) level for S_0 and the lowest triplet state (T_1), while time-dependent DFT (TDDFT)[37] was used for the S_1 state. The CAM-B3LYP exchange–correlation functional[52] was used in combination with the def2-TZVP basis set,[53] and Grimme's D3(BJ) dispersion correction[54] that accounts for van der Waals interactions. The RIJCOSX approxi-

mation[44] was used to accelerate the evaluation of Coulomb and exact exchange integrals.

The structure optimizations and calculations of the excitation energies in the gas phase were carried out with the Turbomole program package.[55,56] The influence of the solid-state environment was modelled by applying a two-layer ONIOM scheme using ORCA.[41–46] The quantum mechanical (QM) region was treated at the TDDFT level, while the environment was described using the semiempirical GFN2-xTB method[45] with electrostatic embedding, as implemented in the *xtb* program.[57]

Excitation energies of the S_1, T_1, and T_2 states were also calculated in the gas phase at the ADC(2) level of theory[47,48] using the def2-TZVP basis set, the molecular structures optimized for the S_1 state in the crystal environment and the reduced-virtual-space (RVS) approach.[58]

In the QM–xTB calculations, a supercell was generated from the experimental unit cell, and hydrogen atom positions were optimized at xTB level. The QM region was then relaxed at the TDDFT level with the xTB region kept frozen. Transition density calculations were carried out at this same level. Spin–orbit coupling (SOC) matrix elements were computed at the TDDFT level using the PySOC and MOLSOC programs.[59,60] The reverse intersystem crossing (k_{RISC}) rate at RT (298 K) was estimated using the approach described by Gadirov *et al.*[40] Environmental effects were not included in the SOC and rate-constant calculations.

Crystallography

The crystals were mounted in inert oil on a MiteGen MicroMount and transferred to the cold nitrogen stream of a Bruker APEX-II CCD diffractometer, equipped with an Oxford Instruments low-temperature controller system (Mo Kα = 0.71073 Å, graphite monochromator). Data were collected in ω- and φ-scan modes. Absorption effects were treated by semiempirical corrections based on multiple scans. The structure was solved with the XT structure solution program using intrinsic phasing and refined on F_0^2 with SHELXL-97.[61] All non-hydrogen atoms were treated anisotropically, and all hydrogen atoms were included as riding bodies. CCDC 2477318–2477320 the supplementary crystallographic data for this paper.

Conclusions

The synthesized bis(diphosphine)-gold(I) complexes **1–4** reported in this work constitute a purposefully designed series of compounds for investigating the TADF phenomena. A detailed photophysical study of the molecules reveals that the observed room-temperature (RT) emissions arise mainly from TADF, with contributions ranging from 67 to 84% depending on the diphosphine ligand. The emission wavelengths of the molecules are affected by the electronic nature of the ligands coordinated to the gold(I) centre. The presence of fused aromatic rings red shifts the emission. The experimental and computational studies suggest that there is a relationship between the structural rigidity of the ligands and the singlet–triplet energy gap ($\Delta E(S_1–T_1)$). Localization of the LUMO on moieties containing aromatic rings appears to be a key factor for strong luminescence.

The combination of the ONIOM embedding scheme and calculations at the *ab initio* correlated ADC(2) level of theory is shown to be a promising computational approach for studying TADF of solid-state materials. ADC(2) calculations on emitter molecules in the gas phase provide results that closely match experimental data when considering the effects of the molecular environment on the molecular structure. The results obtained at the ADC(2) level using the molecular structure of the excited state optimized in TDDFT/ONIOM calculations are significantly more accurate that those obtained in gas-phase studies. The calculated $(S_1|H_{SO}|T_1)$ values show that the spin–orbit coupling is strong, leading to small $\Delta E(S_1–T_1)$ values and large k_{ISC} and k_{RISC} constants. These properties enable a rapid population of the T_1 state upon excitation and an efficient repopulation of the S_1 state leading to the efficient TADF process that is observed for these molecules. The obtained results highlight the crucial role of the molecular structure of the ligands and the molecular environment in tuning photophysical properties. The present study demonstrates the potential of these gold(I) complexes as TADF emitters in OLEDs.

Author contributions

All authors contributed to the writing of the manuscript and approved its final version. The experimental work was conducted by O. B., I. S., M. E. O., M. M., M. R. C. and J. M. L. L., whereas the computational studies were performed by R. T. N., R. R. V. and D. S.

Conflicts of interest

There are no conflicts to declare.

Data availability

The data supporting this article have been included as part of the supplementary information (SI). Supplementary information is available. See DOI: **https://doi.org/10.1039/d5qi01661d**.

CCDC 2477318–2477320 contain the supplementary crystallographic data for this paper.[62a–c]

Acknowledgements

We gratefully acknowledge the DGI MICINN/FEDER (project number PID2022-139739NB-l00 (AEI/FEDER, UE)) and by "ERDF A way of making Europe". O. B. also acknowledges for the FPI grant PRE2022-000198, financed by the MCIN/AEI/10.13039/501100011033 and the FSE+. This work has been

funded by the Government of La Rioja, the Department of Economy, Innovation, Business, and Self-Employment, through the grant for completing the postdoctoral training stage (Resolution 198/2025, 2025–2028 call). The research has also been supported by The Academy of Finland (project number 340583).

References

1 T. Y. Li, S. J. Zheng, P. I. Djurovich and M. E. Thompson, Two-Coordinate Thermally Activated Delayed Fluorescence Coinage Metal Complexes: Molecular Design, Photophysical Characters, and Device Application, *Chem. Rev.*, 2024, **124**, 4332–4392.

2 F. Ni, Y. Huang, L. Qiu and C. Yang, Synthetic progress of organic thermally activated delayed fluorescence emitters via C-H activation and functionalization, *Chem. Soc. Rev.*, 2024, **53**, 5904–5955.

3 V. Ferraro, C. Bizzarri and S. Bräse, Thermally Activated Delayed Fluorescence (TADF) Materials Based on Earth-Abundant Transition Metal Complexes: Synthesis, Design and Applications, *Adv. Sci.*, 2024, **11**, 2404866.

4 R. Czerwieniec, M. J. Leitl, H. H. H. Homeier and H. Yersin, Cu(I) complexes – Thermally activated delayed fluorescence. Photophysical approach and material design, *Coord. Chem. Rev.*, 2016, **325**, 2–28.

5 H. Yersin, R. Czerwieniec, M. Z. Shafikov and A. F. Suleymanova, TADF Material Design: Photophysical Background and Case Studies Focusing on CuI and AgI Complexes, *ChemPhysChem*, 2017, **18**, 3508–3535.

6 J. A. Barltrop and J. D. Coyle, *Excited states in organic chemistry*, Wiley, New York, 1975.

7 P. W. Atkins, *Quanta: A Handbook of Concepts*, Oxford University Press, Oxford, UK, 1991.

8 A. Farokhi, S. Lipinski, L. M. Cavinato, H. Shahroosvand, B. Pashaei, S. Karimi, S. Bellani, F. Bonaccorso and R. D. Costa, Metal complex-based TADF: design, characterization, and lighting devices, *Chem. Soc. Rev.*, 2025, **54**, 266–340.

9 X.-K. Chen, D. Kim and J.-L. Brédas, Thermally Activated Delayed Fluorescence (TADF) Path toward Efficient Electroluminescence in Purely Organic Materials: Molecular Level Insight, *Acc. Chem. Res.*, 2018, **51**, 2215–2224.

10 H. Noda, H. Nakanotani and C. Adachi, Excited state engineering for efficient reverse intersystem crossing, *Sci. Adv.*, 2018, **4**, eaao6910.

11 J. M. López-de-Luzuriaga, M. Monge, M. E. Olmos, M. Rodríguez-Castillo, I. Soldevilla, D. Sundholm and R. R. Valiev, Perhalophenyl Three-Coordinate Gold(I) Complexes as TADF Emitters: A Photophysical Study from Experimental and Computational Viewpoints, *Inorg. Chem.*, 2020, **59**, 14236–14244.

12 I. Soldevilla, A. García-Camacho, R. T. Nasibullin, M. E. Olmos, M. Monge, D. Sundholm, R. R. Valiev, J. M. López-De-Luzuriaga and M. Rodríguez-Castillo, Influence of perhalophenyl groups in the TADF mechanism of diphosphino gold(I) complexes, *J. Mater. Chem. C*, 2022, **10**, 4894–4904.

13 I. Soldevilla, A. G. El-Hachimi, R. Ramazanov, R. R. Valiev, M. E. Olmos, M. Monge, D. Sundholm, M. Rodríguez-Castillo and J. M. López-De-Luzuriaga, Improving the quantum yield of luminescence for three-coordinated gold (I) TADF emitters by exploiting inversion symmetry and using perhaloaryl ligands, *J. Mater. Chem. C*, 2024, **12**, 13255–13267.

14 A. S. Davydov, The Theory of Molecular Excitons, *Sov. Phys. Usp.*, 1964, **7**, 145–178.

15 M. Hesse, H. Meier and B. Zeeh, *Spectroscopic Methods in Organic Chemistry*, Thieme, 2nd edn, 2007.

16 H. Yersin and G. Gliemann, Spectroscopic Studies of $M_x[Pt(CN)_4] \cdot yH_2O$, *Ann. N. Y. Acad. Sci.*, 1978, **313**, 539–559.

17 P. Day, Excitons in One-Dimensional Tetracyanoplatinite Salts, *J. Am. Chem. Soc.*, 1975, **97**, 1588–1589.

18 S. Moreno, D. Royo, A. G. El-Hachimi, M. Rodríguez-Castillo, M. Monge, M. E. Olmos and J. M. López-De-Luzuriaga, Vapochromic behaviour of a gold(I)-lead(II) complex as a VOC sensor, *Dalton Trans.*, 2023, **52**, 17119–17131.

19 J. M. López-de-Luzuriaga, M. Monge, M. E. Olmos, M. Rodríguez-Castillo and I. Soldevilla, Versatile coordinative abilities of perhalophenyl-gold(I) fragments to Xantphos: Influence on the emissive properties, *J. Organomet. Chem.*, 2020, **913**, 121198.

20 H. Schmidbaur, G. Reber, A. Schier, F. E. Wagner and G. Müller, Structural Correlations between trans- and cis-Bis(diphenylphosphino)ethene, Bis(diphenylphosphino) methane and their Chlorogold(I) Complexes, *Inorg. Chim. Acta*, 1988, **147**, 143–150.

21 S. J. Berners-Price, L. A. Colquhoun, P. C. Healy, K. A. Byriel and J. V. Hanna, Copper(I) and Gold(I) Complexes with cis-Bis(diphenyl-phosphino)ethylene. Crystal Structures and ^{31}P Cross-polarization Magic Angle Spinning Nuclear Magnetic Resonance Studies, *J. Chem. Soc., Dalton Trans.*, 1992, 3357–3363.

22 W. Levason, G. Reid and M. Webster, 1,2-Bis(diphenyl phosphino)benzene and two related mono-methiodides, $[o,\text{-}C_6H_4(PR_2)(PR_2Me)]I$ (R = Ph or Me), *Acta Crystallogr., Sect. C: Cryst. Struct. Commun.*, 2006, **62**, o438–o440.

23 S. Hillebrand, J. Bruckmann, C. Krüger and M. W. Haenel, Bidentate Phosphines of heteroarenes: 9,9-Dimethyl-4,5-bis (diphenylphosphino)xanthene, *Tetrahedron Lett.*, 1995, **36**, 75–78.

24 M. Kranenburg, Y. E. M. Van Der Burgt, P. C. J. Kamer, P. W. N. M. Van Leeuwen, K. Goubitz and J. Fraanje, New Diphosphine Ligands Based on Heterocyclic Aromatics Inducing Very High Regioselectivity in Rhodium-Catalyzed Hydroformylation: Effect of the Bite Angle, *Organometallics*, 1995, **14**, 3081–3089.

25 R. D. Jackson, S. James, A. G. Orpen and P. G. Pringle, 1,8-Bis(diphenylphosphino)naphthalene: a rigid chelating,

diphosphine analogue of proton sponge, *J. Organomet. Chem.*, 1993, **458**, 3–4.
26 P. Lai, S. Yoon, Y. Wu and T. S. Teets, Effects of Ancillary Ligands on Deep Red to Near-Infrared Cyclometalated Iridium Complexes, *ACS Org. Inorg. Au*, 2022, **2**, 236–244.
27 R. Czerwieniec and H. Yersin, Diversity of copper(I) complexes showing thermally activated delayed fluorescence: Basic photophysical analysis, *Inorg. Chem.*, 2015, **54**, 4322–4327.
28 M. Osawa, M. A. Aino, T. Nagakura, M. Hoshino, Y. Tanaka and M. Akita, Near-unity thermally activated delayed fluorescence efficiency in three- and four-coordinate Au(I) complexes with diphosphine ligands, *Dalton Trans.*, 2018, **47**, 8229–8239.
29 M. J. Leitl, F. R. Küchle, H. A. Mayer, L. Wesemann and H. Yersin, Brightly blue and green emitting Cu(I) dimers for singlet harvesting in OLEDs, *J. Phys. Chem. A*, 2013, **117**, 11823–11836.
30 A. Schinabeck, N. Rau, M. Klein, J. Sundermeyer and H. Yersin, Deep blue emitting Cu(I) tripod complexes. Design of high quantum yield materials showing TADF-assisted phosphorescence, *Dalton Trans.*, 2018, **47**, 17067–17076.
31 T. Hofbeck, U. Monkowius and H. Yersin, Highly efficient luminescence of Cu(I) compounds: Thermally activated delayed fluorescence combined with short-lived phosphorescence, *J. Am. Chem. Soc.*, 2015, **137**, 399–404.
32 J. Toigo, G. Farias, C. A. M. Salla, L. G. T. A. Duarte, A. J. Bortoluzzi, T. D. Zambon Atvars, B. de Souza and I. H. Bechtold, Speeding-up Thermally Activated Delayed Fluorescence in Cu(I) Complexes Using Aminophosphine Ligands, *Eur. J. Inorg. Chem.*, 2021, **31**, 3177–3184.
33 A. Y. Baranov, A. S. Berezin, D. G. Samsonenko, A. S. Mazur, P. M. Tolstoy, V. F. Plyusnin, I. E. Kolesnikov and A. V. Artem'ev, New Cu(I) halide complexes showing TADF combined with room temperature phosphorescence: the balance tuned by halogens, *Dalton Trans.*, 2020, **49**, 3155–3163.
34 A. D. Becke, Density-fnnctional exchange-energy approximation with correct asymptotic behavior, *Phys. Rev. A*, 1988, **38**, 3098–3100.
35 A. D. Becke, Density-functional thermochemistry. III. The role of exact exchange, *J. Chem. Phys.*, 1993, **98**, 5648–5652.
36 C. Lee, W. Yang and R. G. Parr, Development of the Colic-Salvetti correlation-energy formula into a functional of the electron density, *Phys. Rev. B: Condens. Matter Mater. Phys.*, 1988, **37**, 785–789.
37 M. E. Casida and M. Huix-Rotllant, Progress in Time-Dependent Density-Functional Theory, *Annu. Rev. Phys. Chem.*, 2012, **63**, 287–323.
38 C. C. J. Chiang, A. Kimyonok, M. K. Etherington, G. C. Griffiths, V. Jankus, F. Turksoy and A. P. Monkman, Ultrahigh efficiency fluorescent single and bi-layer organic light emitting diodes: The key role of triplet fusion, *Adv. Funct. Mater.*, 2013, **23**, 739–746.
39 T. J. Penfold, F. B. Dias and A. P. Monkman, The theory of thermally activated delayed fluorescence for organic light emitting diodes, *Chem. Commun.*, 2018, **54**, 3926–3935.
40 R. M. Gadirov, R. R. Valiev, L. G. Samsonova, K. M. Degtyarenko, N. V. Izmailova, A. V. Odod, S. S. Krasnikova, I. K. Yakushchenko and T. N. Kopylova, Thermally activated delayed fluorescence in dibenzothiophene sulfone derivatives: Theory and experiment, *Chem. Phys. Lett.*, 2019, **717**, 53–58.
41 F. Neese, Software update: The ORCA program system, Version 5.0, *Wiley Interdiscip. Rev.: Comput. Mol. Sci.*, 2022, **12**, e1606.
42 F. Neese and G. Olbrich, Efficient use of the resolution of the identity approximation in time-dependent density functional calculations with hybrid density functionals, *Chem. Phys. Lett.*, 2002, **362**, 170–178.
43 F. Neese, An improvement of the resolution of the identity approximation for the formation of the Coulomb matrix, *J. Comput. Chem.*, 2003, **24**, 1740–1747.
44 F. Neese, F. Wennmohs, A. Hansen and U. Becker, Efficient, approximate and parallel Hartree-Fock and hybrid DFT calculations. A 'chain-of-spheres' algorithm for the Hartree-Fock exchange, *Chem. Phys.*, 2009, **356**, 98–109.
45 C. Bannwarth, E. Caldeweyher, S. Ehlert, A. Hansen, P. Pracht, J. Seibert, S. Spicher and S. Grimme, Extended tight–binding quantum chemistry methods, *Wiley Interdiscip. Rev.: Comput. Mol. Sci.*, 2021, **11**, e1493.
46 B. Helmich-Paris, B. de Souza, F. Neese and R. Izsák, An improved chain of spheres for exchange algorithm, *J. Chem. Phys.*, 2021, **155**, 104109.
47 N. O. C. Winter and C. Hättig, Scaled opposite-spin CC2 for ground and excited states with fourth order scaling computational costs, *J. Chem. Phys.*, 2011, **134**, 184101.
48 N. O. C. Winter and C. Hättig, Quartic scaling analytical gradients of scaled opposite-spin CC2, *Chem. Phys.*, 2012, **401**, 217–227.
49 S. J. Strickler and R. A. Berg, Relationship between absorption intensity and fluorescence lifetime of molecules, *J. Chem. Phys.*, 1962, **37**, 814–822.
50 R. Usón, A. Laguna and J. Vicente, Preparation and Properties of Stable Salts Containing Mono- or Bis-(pentafluoro phenyl)aurate(I) and Mono-, Tris-, or Tetrakis-(pentafluoro phenyl)aurate(III) Ions, *J. Chem. Soc., Chem. Commun.*, 1976, 353–354.
51 R. Usón, A. Laguna and J. Vicente, Novel Anionic Gold(I) and Gold(III) Organocomplexes, *J. Organomet. Chem.*, 1977, **131**, 471–475.
52 T. Yanai, D. P. Tew and N. C. Handy, A new hybrid exchange-correlation functional using the Coulomb-attenuating method (CAM-B3LYP), *Chem. Phys. Lett.*, 2004, **393**, 51–57.
53 F. Weigend and R. Ahlrichs, Balanced basis sets of split valence, triple zeta valence and quadruple zeta valence quality for H to Rn: Design and assessment of accuracy, *Phys. Chem. Chem. Phys.*, 2005, **7**, 3297–3305.

54 S. Grimme, S. Ehrlich and L. Goerigk, Effect of the damping function in dispersion corrected density functional theory, *J. Comput. Chem.*, 2011, **32**, 1456–1465.
55 TURBOMOLE V7.7.1. 2023, a Development of University of Karlsruhe and Forschungszentrum Karlsruhe GmbH, 1989–2007, TURBOMOLE GmbH, since 2007; Available from **https://www.turbomole.org** (accessed May 2025).
56 S. G. Balasubramani, G. P. Chen, S. Coriani, M. Diedenhofen, M. S. Frank, Y. J. Franzke, F. Furche, R. Grotjahn, M. E. Harding, C. Hättig, A. Hellweg, B. Helmich-Paris, C. Holzer, U. Huniar, M. Kaupp, A. Marefat Khah, S. Karbalaei Khani, T. Müller, F. Mack, B. D. Nguyen, S. M. Parker, E. Perlt, D. Rappoport, K. Reiter, S. Roy, M. Rückert, G. Schmitz, M. Sierka, E. Tapavicza, D. P. Tew, C. van Wüllen, V. K. Voora, F. Weigend, A. Wodyński and J. M. Yu, TURBOMOLE: Modular program suite for ab initio quantum-chemical and condensed-matter simulations, *J. Chem. Phys.*, 2020, **152**, 184107.
57 C. Bannwarth, S. Ehlert and S. Grimme, GFN2-xTB - An Accurate and Broadly Parametrized Self-Consistent Tight-Binding Quantum Chemical Method with Multipole Electrostatics and Density-Dependent Dispersion Contributions, *J. Chem. Theory Comput.*, 2019, **15**, 1652–1671.
58 R. Send, V. R. I. Kaila and D. Sundholm, Reduction of the virtual space for coupled-cluster excitation energies of large molecules and embedded systems, *J. Chem. Phys.*, 2011, **134**, 214114.
59 X. Gao, S. Bai, D. Fazzi, T. Niehaus, M. Barbatti and W. Thiel, Evaluation of Spin-Orbit Couplings with Linear-Response Time-Dependent Density Functional Methods, *J. Chem. Theory Comput.*, 2017, **13**, 515–524.
60 S. G. Chiodo and M. Leopoldini, MolSOC: A spin–orbit coupling code, *Comput. Phys. Commun.*, 2014, **185**, 676–683.
61 G. M. Sheldrick, *SHELXL-97: Program for Crystals Structure Refinement*, University of Göttingen, Göttingen, Germany, 1997.
62 (*a*) CCDC 2477318: Experimental Crystal Structure Determination, 2025, DOI: **10.5517/ccdc.csd.cc2p4vh6**; (*b*) CCDC 2477319: Experimental Crystal Structure Determination, 2025, DOI: **10.5517/ccdc.csd.cc2p4vj7**; (*c*) CCDC 2477320: Experimental Crystal Structure Determination, 2025, DOI: **10.5517/ccdc.csd.cc2p4vk8**.

